Numerical simulation of macrosegregation in steel ingots using a two-phase model

Wen-sheng Li, Hou-fa Shen, and Bai-cheng Liu

The Key Laboratory of the Ministry of Education of China for Advanced Materials Processing Technology, Department of Mechanical Engineering, Tsinghua University, Beijing 100084, China

(Received: 13 October 2011; revised: 26 October 2011; accepted: 12 November 2011)

Abstract: A two-phase model for the prediction of macrosegregation formed during solidification is presented. This model incorporates the descriptions of heat transfer, melt convection, solute transport, and solid movement on the system scale with microscopic relations for grain nucleation and growth. Then the model is used to simulate the solidification of a benchmark industrial 3.3-t steel ingot. Simulations are performed to investigate the effects of grain motion and pipe shrinkage formation on the final macrosegregation pattern. The model predictions are compared with experimental data and numerical results from literatures. It is demonstrated that the model is able to express the overall macrosegregation patterns in the ingot. Furthermore, the results show that it is essential to consider the motion of equiaxed grains and the formation of pipe shrinkage in modelling. Several issues for future model improvements are identified.

Keywords: steel ingots; solidification; segregation; shrinkage; modelling

---

Nomenclature

c: Specific heat capacity, $\text{J·kg}^{-1}\text{·K}^{-1}$;

C: Concentration of carbon, wt%;

d_s: Grain diameter, m;

D: Mass diffusivity, $\text{m}^2\text{·s}^{-1}$;

g: Volume fraction;

g_c: Grain packing limit;

$\boldsymbol{g}$: Gravity vector, m·s^{-2};

k_p: Partition ratio;

k: Thermal conductivity, $\text{W·m}^{-1}\text{·K}^{-1}$;

L: Latent heat, J·kg^{-1};

m_l: Liquidus slope, $\text{K·wt\%}^{-1}$;

N: Grain production rate, $\text{m}^{-3}\text{·s}^{-1}$;

n: Grain density, m^{-3};

n_{max}: Maximum grain density, m^{-3};

p: Pressure, N·m^{-2};

Re: Reynolds number;

S_v: Interfacial area concentration, m^{-1};

t: Time, s;

T: Temperature, °C;

T_m: Melting point of pure iron, °C;

$\boldsymbol{u}$: Velocity vector, m·s^{-1}.

β: Drag coefficient, $\text{kg·m}^{-3}\text{·s}^{-1}$;

β_{sl}: Solidification volume shrinkage;

β_C: Solutal expansion coefficient, $\text{wt\%}^{-1}$;

β_T: Thermal expansion coefficient, K^{-1};

$\varGamma$: Interfacial phase change rate, $\text{kg·m}^{-3}\text{·s}^{-1}$;

δ: Solute diffusion length, m;

Ⓐ Springer

788

Int. J. Miner. Metall. Mater., Vol.19, No.9, Sep 2012

ΔT: Undercooling, K;

ΔT_N: Undercooling for maximum grain production rate, K;

ΔT_σ: Gaussian distribution width of the nucleation law, K;

μ: Dynamic viscosity, kg·m^{-1}·s^{-1};

ρ: Density, kg·m^{-3}.

Subscripts or superscripts

0: Initial;

b: Buoyancy;

l: Liquid phase;

ref: Reference;

s: Solid phase;

*: Equilibrium at the solid-liquid interface.

1. Introduction

Macrosegregation in large steel ingots has long been a topic of engineering importance [1]. The typical macrosegregation patterns in steel ingots consist of a positively segregated zone at the top of the ingots and a negative segregation cone at the bottom [2-4]. It is well established that the main causes of macrosegregation include melt flow induced by thermosolutal convection and shrinkage and the motion of free equiaxed grains. Modelling macrosegregation is a multiphase and multiscale problem. Beckermann and co-workers [5-6] were the first to present multiphase models that account for melt convection and solid movement. The global transport phenomena at the process scale and the grain nucleation and growth mechanisms on a microscopic scale are bridged in these pioneering models. Ludwig and co-workers [7-10] developed a series of multiphase models which are of a more advanced nature. The most sophisticated one is a five-phase model for mixed columnar-equiaxed solidification that tracks the evolution of dendritic morphologies, encompasses melt convection and sedimentation of equiaxed grains, and allows the prediction of the macrostructure and the macrosegregation [10]. Combeau and co-workers [11-12] presented a multiphase and multiscale solidification model which describes the morphology evolution of equiaxed grains and their motion. In addition, a brief description of some other multiphase models can be found in a recent and well-documented review [13].

The application of these sophisticated models to industrial steel ingots is limited mainly because of the large computational resources required to accurately resolve the variety of the phenomena over the process scale [14]. Combeau and co-workers [11, 15] simulated the solidification of a 3.3-t steel ingot, using a fully coupled multiphase and multiscale model. This work represents a pioneering application of such a model to an industrial-sized production steel ingot [15]. Furthermore, the experimental results of a carbon segregation map for a longitudinal section of the ingot was presented [11]. This map was constructed from composition measurements by an intercept method in 114 sampling points. Such detailed measurements for validating the prediction of macrosegregation in steel ingots are seldom available in literatures.

In this paper, a two-phase multiscale model was proposed to simulate the solidification of the benchmark 3.3 t steel ingot. The model involves the simultaneous consideration of the coupled macroscopic phenomena of heat transfer, fluid flow, solute transport and solid movement, and the microscopic phenomena of grain nucleation and growth. The macrosegregation predictions under two possible assumptions on the motion of the solid phase (fixed solid phase or moving grains) were presented and discussed. Furthermore, the formation of shrinkage cavity in the hot-top was simulated, and its influence on macrosegregation was also investigated. The results were compared with experimental data and simulation results from Ref. [11]. The present study may shed new light on the potential of the advanced models for predicting macrosegregation in industrial steel ingots.

2. Model

The model proposed in this paper is developed based on a volume-averaged Euler-Euler two-phase formulation. Indeed, the present model is a modification and continuation of the previous multiphase multiscale solidification models of Beckermann and co-workers [5-6], Ludwig and Wu [7], and Založnik and Combeau [12]. The model equations and supplementary relations are summarized in Tables 1 and 2, respectively. The basic concepts of volume averaging and the derivation of the model are detailed elsewhere [5-7, 12] and, hence, only a few explanations are included here.

The main assumptions employed in the present model are as follows.

(1) The physical system considered consists of solid (s) and liquid (l) phases. The volume fractions, g_s and g_l, are subject to $g_s+g_l=1$.

Table 1.   Two-phase model

Mass conservation	$\dfrac{\partial}{\partial t}\left(g_s\rho_s\right)+\nabla\cdot\left(g_s\rho_s\boldsymbol{u}_s\right)=\varGamma_s$	(1)
	$\dfrac{\partial}{\partial t}\left(g_l\rho_l\right)+\nabla\cdot\left(g_l\rho_l\boldsymbol{u}_l\right)=-\varGamma_s$	(2)
Momentum conservation	$\dfrac{\partial}{\partial t}\left(g_s\rho_s\boldsymbol{u}_s\right)+\nabla\cdot\left(g_s\rho_s\boldsymbol{u}_s\boldsymbol{u}_s\right)=-g_s\nabla p+\nabla\cdot\left(\mu_s g_s\nabla\boldsymbol{u}_s\right)+g_s\rho_s^b\boldsymbol{g}+\beta(\boldsymbol{u}_l-\boldsymbol{u}_s)$	(3)
	$\dfrac{\partial}{\partial t}\left(g_l\rho_l\boldsymbol{u}_l\right)+\nabla\cdot\left(g_l\rho_l\boldsymbol{u}_l\boldsymbol{u}_l\right)=-g_l\nabla p+\nabla\cdot\left(\mu_l g_l\nabla\boldsymbol{u}_l\right)+g_l\rho_l^b\boldsymbol{g}+\beta(\boldsymbol{u}_s-\boldsymbol{u}_l)$	(4)
Species conservation	$\dfrac{\partial}{\partial t}\left(g_s\rho_s C_s\right)+\nabla\cdot\left(g_s\rho_s\boldsymbol{u}_s C_s\right)=\dfrac{S_V\rho D_s}{\delta_s}(C_s^*-C_s)+C_s^*\varGamma_s$	(5)
	$\dfrac{\partial}{\partial t}\left(g_l\rho_l C_l\right)+\nabla\cdot\left(g_l\rho_l\boldsymbol{u}_l C_l\right)=-\left[\dfrac{S_V\rho D_s}{\delta_s}(C_s^*-C_s)+C_s^*\varGamma_s\right]$	(6)
Energy conservation	$\dfrac{\partial}{\partial t}[(g_s\rho_s c_s+g_l\rho_l c_l)T]+\nabla\cdot[(g_s\rho_s c_s\boldsymbol{u}_s+g_l\rho_l c_l\boldsymbol{u}_l)T]=\nabla\cdot[(g_s k_s+g_l k_l)\nabla T]+\varGamma_s L$	(7)
Interfacial species balance	$\dfrac{S_V\rho D_s}{\delta_s}(C_s^*-C_s)+C_s^*\varGamma_s+\dfrac{S_V\rho D_l}{\delta_l}(C_l^*-C_l)-C_l^*\varGamma_s=0$	(8)

Table 2.   Supplementary relations

Grain density	$\dfrac{\partial}{\partial t}n+\nabla\cdot\left(\boldsymbol{u}_s n\right)=N$	(9)
Nucleation model	$N=\dfrac{\mathrm{d}\Delta T}{\mathrm{d}t}\dfrac{n_{max}}{\sqrt{2\pi}\Delta T_\sigma}\mathrm{e}^{-\frac{1}{2}\left(\frac{\Delta T-\Delta T_N}{\Delta T_\sigma}\right)^2}$	(10)
Density	$\rho_s=\rho_l=\rho=\rho_{ref}$	(11)
	$\rho_s^b=\rho_{ref}(1+\beta_{sl})$, $\rho_l^b=\rho_{ref}[1-\beta_T(T-T_{ref})-\beta_C(C_l-C_{ref})]$	(12)
Drag coefficient	$\beta=\begin{cases}\dfrac{3}{4}C_D\dfrac{g_s g_l\rho_l}{d_p}\left|\boldsymbol{u}_s-\boldsymbol{u}_l\right|g_l^{-2.65}, & g_s\le0.2\\[2ex]150\dfrac{g_s^2\mu_l}{g_l d_p^2}+1.75\dfrac{\rho_l g_s}{d_p}\left|\boldsymbol{u}_s-\boldsymbol{u}_l\right|, & g_s>0.2\end{cases}$	(13)
	$C_D=\begin{cases}(24/Re)(1+0.15Re^{0.687}), & Re<1000\\0.44, & Re\ge1000\end{cases}\quad Re=\dfrac{g_l\rho_l d_p}{\mu_l}\left|\boldsymbol{u}_s-\boldsymbol{u}_l\right|$	(14)
Interfacial solute diffusion lengths	$\delta_s=\dfrac{d_s}{10}$, $\delta_l=\dfrac{d_s}{2}$	(15)
Microstructural dimensions	$d_s=\sqrt[3]{6g_s/(n\pi)}$, $S_V=n\pi d_s^2$	(16)
Interfacial equilibrium relations	$C_s^*=k_p C_l^*$, $T=T_m+m_l C_l^*$	(17)
Solid viscosity	$\mu_s=\dfrac{\mu_l}{g_s}[(1-g_s/g_c)^{-2.5g_c}-(1-g_s)]$	(18)

(2) The solid is presented in the form of free equiaxed (globular) grains or a continuous structure packed by the interacted and merged grains. The size of equiaxed grains are explicitly calculated, while a constant value for the secondary arm spacing of columnar dendrites (*i.e.*, continuous structure) is assumed.

(3) Solid and liquid densities are assumed equal and constant, except in the buoyancy term of the momentum conservation equation. The Boussinesq approximation is employed to model the thermosolutal convection, grain sedimentation, and the induced melt convection.

(4) Mold filling is not simulated. Equiaxed grains or solid fragments that have separated from a mould wall or free surface or melted off dendrites are not modeled.

The interfacial drag force is modeled using the Gidaspow model [16], which employs the Wen and Yu model for low solid fractions (*i.e.*, the free particle regime) and applies the Ergun model for high solid fractions (*i.e.*, the packed bed regime). The drag coefficient for a single sphere (the well-known Stokes law) and the Kozeny-Carman perme-

ability relation for a packed bed of spheres could be viewed as the simplified, limiting cases of the present interfacial drag correlation. It should be noted that the momentum equations of two phases, solid and liquid, are valid for all solid fractions ranging from zero to unity. Thus, the packing limit is considered in the expression for the effective solid viscosity (Eq. (18) in Table 2). As soon as the solid fraction reaches the packing limit, the solid will become rigid and fixed.

The local thermal equilibrium is assumed. The interfacial species balance in Table 1 constitutes the grain growth model, with the interfacial species diffusion lengths shown in Table 2. In addition, a three-parameter heterogeneous nucleation law (Eq. (10) in Table 2) is used to model the grain nucleation [7].

The conservation equations are discretized using a control volume-based finite difference method. The transient term is treated fully implicit. For discretizing the momentum equations, a staggered grid is adopted. The sparse linear systems of discretized equations are solved by the SIP (strongly implicit procedure) method [17]. An extension of the well-known single-phase solution algorithm SIMPLE (semi-implicit method for pressure-linked equations) [18] to multiphase flows, called the IPSA (inter-phase slip algorithm), is employed in the present two-phase model. A detailed description of this algorithm is given by Karema and Lo [19].

The formation of a shrinkage cavity at the top of the ingot can be calculated following the approaches in Refs. [20-21]. The basic concept is that the total shrinkage volume of the ingot for each time step during solidification is equal to the sum of solidification contraction of all the elements. Once the total shrinkage amount is larger than the volume of one single element, numbers of elements that (1) are the closest to the top and centre of the ingot domain and (2) have a solid fraction less than the critical solid fraction (assigned 0.35 in the present study), must be treated as empty. The thermophysical properties of the empty element are considered to be those of the ambient (*i.e.*, exothermic powder), and the corresponding boundary conditions are updated.

3. Results and discussion

The steel ingot simulated in the present study is shown in Fig. 1. It was a 3.3-t ingot of 2 m in height and 0.6 m in mean width, of which comprehensive experimental measurements and other details were reported by Combeau *et al.* [11]. Two-dimensional simulations were carried out. The

computational domain was meshed into volume elements of 10 mm×15 mm. The time-step was variable, in the order of 0.01 s.
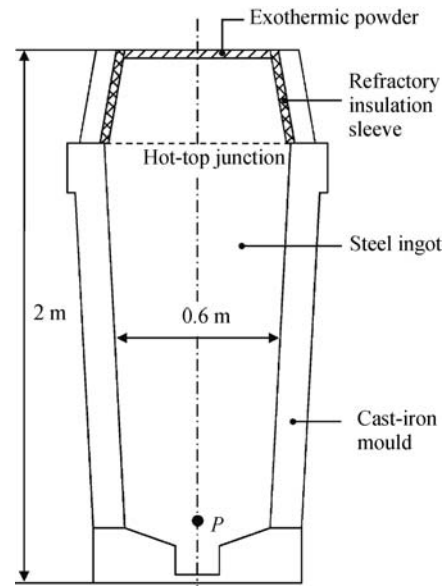

Fig. 1.   Schematic of the 3.3-t steel ingot simulated in the present study.

To illustrate the effects of grain motion and shrinkage cavity formation on the macrosegregation in the ingot, three cases were investigated.

(1) Case 1. The solid phase was fixed everywhere, allowing thermosolutal convection for the melt in the pure liquid region and the stationary mush zone. This was implemented in the model by setting the packing limit g_c=0. Shrinkage was not simulated.

(2) Case 2. Solid movement was considered with a packing limit of g_c=0.2.

(3) Case 3 is basically the same as case 2, but the formation of shrinkage cavity at the top of the ingot was calculated.

In order to account for the columnar zone observed experimentally, the grains were imposed to be fixed within a layer of approximately 6 cm in width at the mould walls [11], in all cases.

The steel properties and other parameters used in the simulations are summarized in Table 3. The thermophysical properties of the mould materials as well as the initial and boundary conditions are essentially identical to those listed in Ref. [22] and are not repeated here. It should be pointed out that a characterized particle diameter d_p is introduced in the drag coefficient expression (Eq. (13) in Table 2). For a solid fraction greater than the packing limit, d_p is equivalent to the

Table 3.   Thermophysical properties and parameters used in the present simulations

C_0 / wt%	T_m / °C	m_l / (K·wt%$^{-1}$)	k_p	L / (J·kg^{-1})	μ_l / (kg·m^{-1}·s^{-1})	D_l / (m^2·s^{-1})	D_s / (m^2·s^{-1})
0.36	1532	−80.45	0.314	2.71×10^5	4.2×10^{-3}	2×10^{-8}	5.187×10^{-11}

SDAS / μm	ρ_{ref} / (kg·m^{-3})	β_{sl}	β_C / wt%$^{-1}$	β_T / K^{-1}	n_{max} / m^{-3}	ΔT_N / K	ΔT_σ / K
300	6990	0.045	1.4164×10^{-2}	1.07×10^{-4}	5×10^{12}	5	2

secondary dendrite arm spacing (SDAS); otherwise it equals to the grain diameter d_s.

3.1. Case 1

The predicted solidification sequences of the ingot are shown in Fig. 2. At 600 s (Fig. 2(a)), the melt at the mould side has a higher density because of the lower temperature and, thus, the thermal buoyancy force acts downward. In the top two-thirds of the ingot, where no significant solutal gradients are established, a descending melt flows along the mould side can be observed. Consequently, this flow induces an upward melt flow in the ingot centre and, hence, consists of a counterclockwise convection cell. In the bottom one-thirds of the ingot, however, there exists a layer of enriched liquid (marked with a segregation ratio, $(C−C_0)/C_0$, of 0.005 in Fig. 2(a)) in front of the mushy zone. Because

the solute-enriched interdendritic melt has a lower density, the solutal buoyancy points upward. Since the thermophysical parameters used in the simulation indicates that the solutal buoyancy dominates over the thermal buoyancy, a weak clockwise convection cell in the ingot bottom is expected. As solidification proceeds, at 1200 s, the ingot core is generally positively segregated (also indicated with a segregation ratio of 0.005 in Fig. 2(b)). The stable situation is that the combined thermosolutal buoyancy drives the melt flow upward along the mould side and downward in the ingot centre. Thus, a global clockwise convection cell can be seen in Figs. 2(b) and 2(c). It should be mentioned that at 600 s, the maximum velocity of the melt reaches 11.1 mm·s^{-1}; as solidification proceeds, the melt velocities decrease significantly, of which the maximum magnitude are 5.6 and 0.6 mm·s^{-1} at 1200 and 3600 s, respectively.
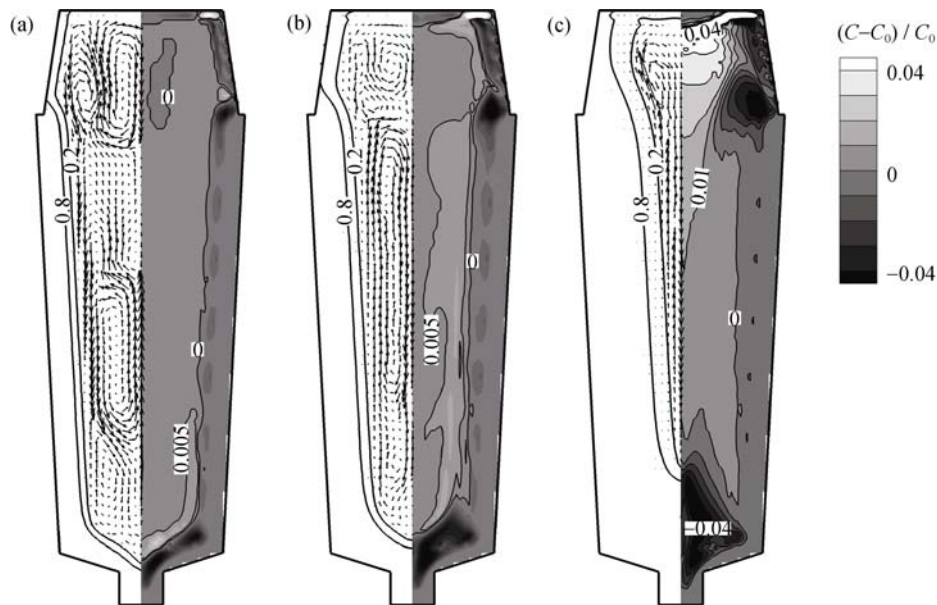

Fig. 2.   Model results in case 1 (left: liquid velocity field and solid fraction contours; right: macrosegregation distribution): (a) 600 s; (b) 1200 s; (c) 3600 s.

As mentioned by Combeau *et al.* [11], the observed segregation tendency can be estimated by the direction of the flow circulation relative to the temperature gradient. At the bottom of the ingot, a clockwise circulation is always presented. This means that the flow is locally oriented in the opposite direction of the temperature gradient and, thus,

leads to a negative segregation. Corresponding to the solid fraction contours, which would indicate a shape of the liquid pool or the fully solidified region, a conically shaped negative segregation zone evolves at the ingot bottom. Consequently, the clockwise circulation brings the solute-rich melt out of the mushy zone, leading to a continual enrichment of

the remaining melt in the ingot core. Hence, the region in and near the centreline of the hot top (the last part to solidify) presents the highest positive segregation.

Fig. 3 shows the predicted evolution of the solid fraction and the segregation ratio at a point, located in the bottom part of the ingot at the centreline, 200 mm above the ingot bottom face (termed point P, illustrated in Fig. 1). At the beginning, this point is in the pure liquid region and has a slight positive segregation. This is also in accordance with that mentioned above and shown in Fig. 2(a). The solidification of this point starts at approximately 800 s. As solidification proceeds, a negative segregation tendency establishes because of the flow direction and the opposite temperature gradient. Finally, this point exhibits a negative segregation.
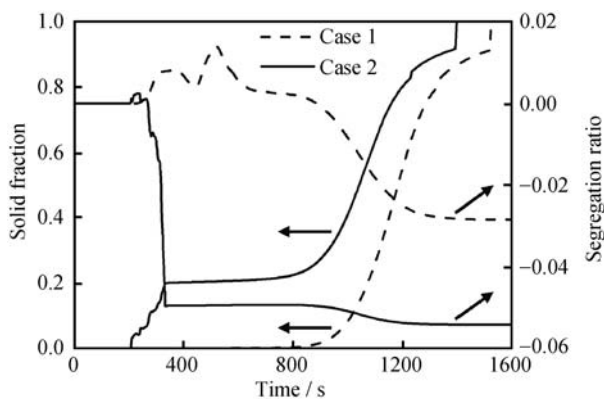

Fig. 3. Predicted evolution of solid fraction and the segregation ratio at a point located at the centerline and 200 mm above the bottom face of the ingot.

The present flow structure and macrosegregation pattern in the ingot are equivalent to those in a previous study [22] in which a continuum model of the classic mixture theory was used. While the thermal buoyancy dominates over the solutal buoyancy, in the preceding work of Gu and Beckermann [21], a counterclockwise-flow circulation was predicted. The discrepancy in flow patterns can be attributed to the varied values of the thermal and solutal expansion coefficients used. Indeed, the formation mechanisms of the flow and the macrosegregation would be fundamentally the same.

3.2. Case 2

This case considers both melt convection and solid movement during solidification. Fig. 4 presents the solidification and transport behaviors at 600, 1200, and 3600 s, respectively. After the formation of the columnar layer at the surface, the equiaxed grains nucleated are free to move. Because solid is heavier than liquid and the interfacial drag is considered dependent on the grain size, larger grains have stronger tendencies to settle. Hence, the grains descend along the columnar zone and entrain the surrounding liquid with them, inducing a downward melt flow at the mould side and an upward one in the ingot centre (*i.e.*, a counterclockwise convection cell). As the grains settle, they are blocked when the local solid fraction exceeds the packing limit and, thus, solid accumulates at the ingot bottom. It can be observed in Figs. 4(a) and 4(b) that the ingot core is filled up with the packed grains; correspondingly, the fully solidified layer along the surface only evolves slowly into the centre.
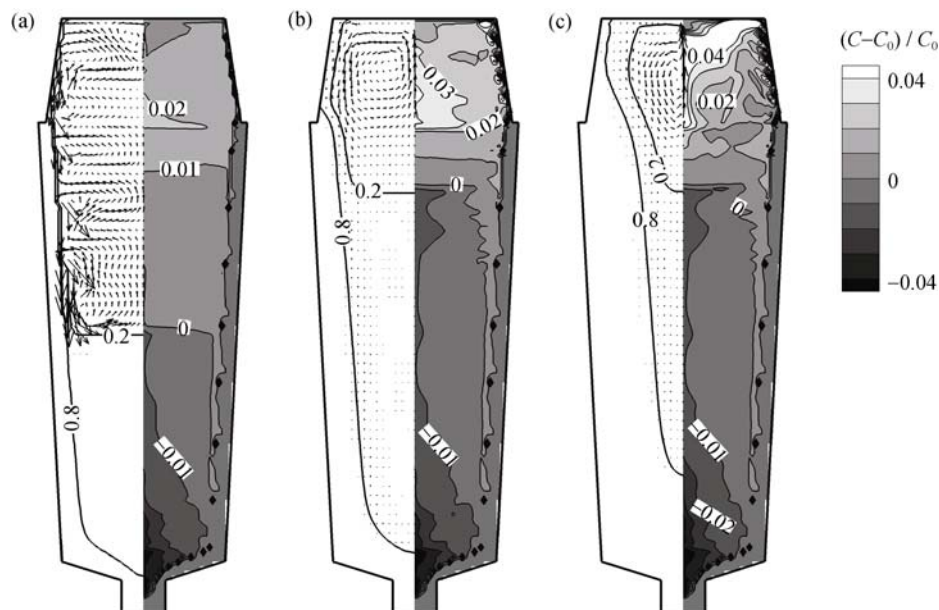

Fig. 4. Model results in case 2 (left: liquid velocity field and solid fraction contours; right: macrosegregation distribution): (a) 600 s; (b) 1200 s; (c) 3600 s.

In the porous region ($g_s > g_c$), although the liquid can penetrate through the stationary packed bed of grains, these liquid velocities cannot be seen in Fig. 4(a) or are negligible in Figs. 4(b) and 4(c) because of the large velocity scale used in these figures. In the slurry region ($g_s < g_c$), where solid grains are considered to freely move, the downward component of the solid velocity is only a little larger than the one of the liquid. Hence, the relative velocities between two phases are generally small compared with either the solid or the liquid velocity. Actually, the velocity vectors of the solid phase are similar to those of the liquid phase to some extent and, thus, are not illustrated in Fig. 4.

As shown in Fig. 3, for point *P* in the bottom part of the ingot, the increase in solid fraction and the decrease in composition with time are characterized by two distinct stages. The first stage corresponds to the period of grain sedimentation. The decisive negative segregation forms in this stage because of the settling of the globular, solute-lean grains. The second stage begins at approximately 330 s, when the solid fraction approaches the packing limit. Because there is no significant interdendritic liquid flow in the packed layer, only a small additional change in the macrosegregation of point *P* takes place during this long period.

3.3. Case 3

Based on case 2, it is of interest to further investigate the macrosegregation in the ingot when the pipe shrinkage formation is considered. Not surprisingly, the global solidification and transport behaviors (case 3) are very similar to case 2. The final macrosegregation pattern, together with a brief discussion, is presented in the following section.

3.4. Comparison of final macrosegregation patterns

Fig. 5 shows the predicted final macrosegregation patterns of carbon in cases 1-3. In all simulations, a positive segregation was predicted in the hot top part and a conically shaped negative segregation zone was predicted at the bottom of the ingot. In case 1 (Fig. 5(a)), there is a negative segregation region in the side and bottom of the hot top part; and the most serious negative segregation at the ingot bottom is located a little off the centreline. In case 2 (Fig. 5(b)), in which the interdendritic liquid flow is somewhat weaker and a global vertical segregation gradient is more prone to exist because of grain settling, the hot-top negative segregation is absent. Furthermore, the most prominent negative segregation is located at the centreline in the bottom part of the ingot. In case 3 (Fig. 5(c)), the overall macrosegregation pattern is very similar to case 2, except that the positive segregation zone is gently shifted downwards to the hot-top junction because of the pipe formation. It should be noted that the lack of experimental data prevents the validation of the predictions for the shape and depth of the pipe shrinkage.
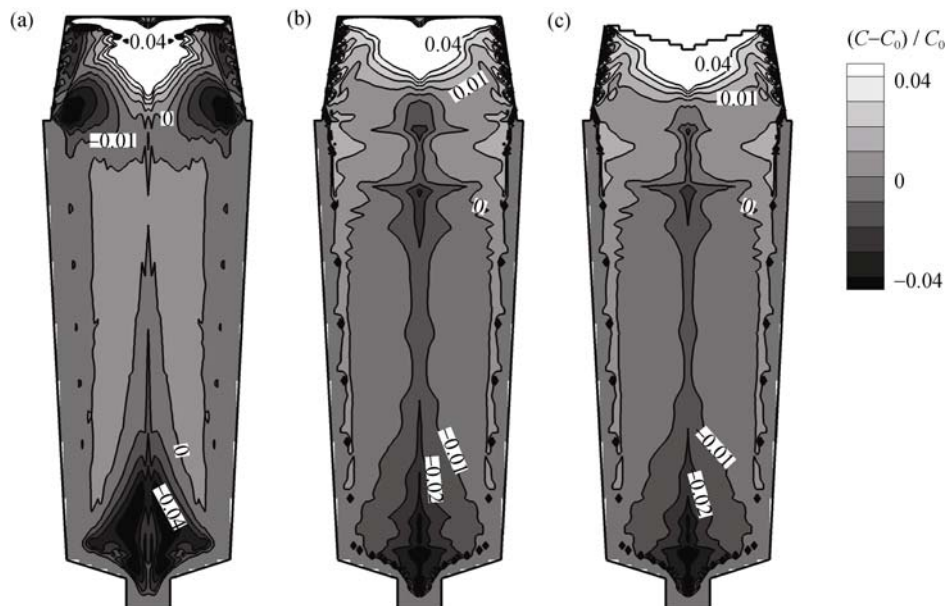

Fig. 5.   Predicted final macrosegregation patterns in three cases: (a) case 1; (b) case 2; (c) case 3.

Fig. 6 shows a comparison of the measured and the predicted carbon macrosegregation along the vertical centreline of the ingot. The experimental data and the model results for a fixed solid phase [11] serve as crucial bases for validating the present model. In general, the agreement among the results plotted can be considered good. However, the present predictions for the positive hot-top segregation are underestimated as compared to the measurements. Furthermore, the

most obvious difference between the numerical results is found below the hot-top junction and takes up approximately one-third of the ingot height. For this segment, there is a large oscillation in both the measured and the predicted segregation ratios [11], with a maximum positive value of about 0.1; the predicted concentration in case 1 is close to the nominal one, and cases 2-3 exhibit a negative segregation tendency. For the entire ingot height, however, the simulation with solid movement and pipe formation (case 3) appears to provide the best prediction of the segregation tendency. Nonetheless, further modelling refinements and detailed experimental validations are still required.
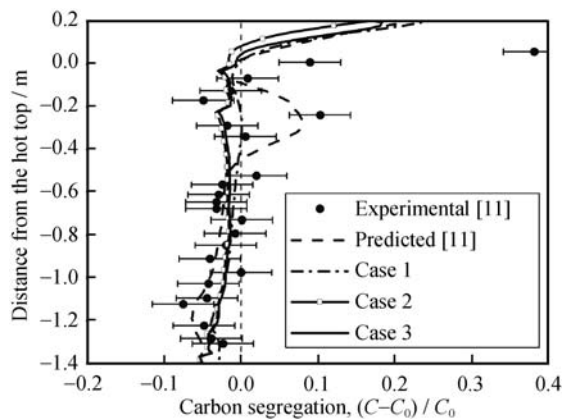

Fig. 6. Comparison of the variation in measured and predicted macrosegregation along the centreline of the ingot.

4. Conclusions

A two-phase solidification model has been proposed to predict macrosegregation in steel ingots. The model incorporates heat transfer, melt convection, solute transport, and solid movement on the system scale, and nucleation and interfacial drag on a microscopic scale. It was used to simulate the solidification of a benchmark industrial 3.3-t steel ingot. Results of three different simulations were presented. Comparisons with prior experimental and numerical results in Ref. [11] were also performed. Positive segregation was predicted in the hot top and a conically shaped negative segregation zone was predicted at the bottom of the ingot. It was demonstrated that the macrosegregation could be reproduced rather well in the simulation where grain motion and pipe shrinkage formation was taken into account. Nevertheless, the present model should only be viewed as a simplified version when compared to published sophisticated models. More detailed consideration of the microstructure and grain transitions is needed in modelling. Microscale parameters such as grain density, interfacial drag coefficients, and local diffusion lengths should also be determined with more accuracy. In addition, experimental validation is an important future research issue.

References

[1] M.C. Flemings, Principles of control of soundness and homogeneity of large ingots, *Scand. J. Metall.*, 5(1976), p.1.

[2] M.C. Flemings, Our understanding of macrosegregation: Past and present, *ISIJ Int.*, 40(2000), No.9, p.833.

[3] C. Beckermann, Modelling of macrosegregation: Applications and future needs, *Int. Mater. Rev.*, 47(2002), No.5, p.243.

[4] G. Lesoult, Macrosegregation in steel strands and ingots: Characterisation, formation and consequences, *Mater. Sci. Eng. A*, 413-414(2005), p.19.

[5] J. Ni and C. Beckermann, A volume-averaged two-phase model for transport phenomena during solidification, *Metall. Trans. B*, 22(1991), p.349.

[6] C.Y. Wang and C. Beckermann, Equiaxed dendritic solidification with convection: Part I. Multiscale/multiphase modeling, *Metall. Mater. Trans. A*, 27(1996), p.2754.

[7] A. Ludwig and M. Wu, Modeling of globular equiaxed solidification with a two-phase approach, *Metall. Mater. Trans. A*, 33(2002), p.3673.

[8] M. Wu and A. Ludwig, A three-phase model for mixed columnar-equiaxed solidification, *Metall. Mater. Trans. A*, 37(2006), p.1613.

[9] M. Wu and A. Ludwig, Modeling equiaxed solidification with melt convection and grain sedimentation: I. Model description, *Acta Mater.*, 57(2009), p.5621.

[10] M. Wu, A. Fjeld, and A. Ludwig, Modelling mixed columnar-equiaxed solidification with melt convection and grain sedimentation: Part I. Model description, *Comput. Mater. Sci.*, 50(2010), p.32.

[11] H. Combeau, M. Založnik, S. Hans, and P.E. Richy, Prediction of macrosegregation in steel ingots: Influence of the motion and the morphology of equiaxed grains, *Metall. Mater. Trans. B*, 40(2009), p.289.

[12] M. Založnik and H. Combeau, An operator splitting scheme for coupling macroscopic transport and grain growth in a two-phase multiscale solidification model: Part I. Model and solution scheme, *Comput. Mater. Sci.*, 48(2010), p.1.

[13] R. Pardeshi, P. Dutta, and A.K. Singh, Modeling of convection and macrosegregation through appropriate consideration of multiphase/multiscale phenomena during alloy solidification, *Ind. Eng. Chem. Res.*, 48(2009), No.19, p.8789.

[14] B.C. Liu, Q.Y. Xu, T. Jing, H.F. Shen, and Z.Q. Han, Advances in multi-scale modeling of solidification and casting processes, *JOM*, 63(2011), No.4, p.19.

[15] H. Combeau, A. Kumar, and M. Založnik, Modeling of equiaxed grain evolution and macrosegregations development in steel ingots, *Trans. Indian Inst. Met.*, 62(2009), p.285.

[16] D. Gidaspow, *Multiphase Flow and Fluidization, Continuum and Kinetic Theory Description*, Academic Press, New York, 1994, p.35.

[17] J.H. Ferziger and M. Peric, *Computational Methods for Fluid Dynamics*, Springer, New York, 2002, p.101.

[18] S.V. Patankar, *Numerical Heat Transfer and Fluid Flow*, Hemisphere, New York, 1980, p.113.

[19] H. Karema and S. Lo, Efficiency of interphase coupling algorithms in fluidized bed conditions, *Comput. Fluids*, 28(1999), p.323.

[20] B.C. Liu, H.F. Shen, and W.Z. Li, Progress in numerical simulation of solidification process of shaped casting, *J. Mater. Sci. Technol.*, 11(1995), p.313.

[21] J.P. Gu and C. Beckermann, Simulation of convection and macrosegregation in a large steel ingot, *Metall. Mater. Trans. A*, 30(1999), p.1357.

[22] W.S. Li, H.F. Shen, and B.C. Liu, Three-dimensional simulation of thermosolutal convection and macrosegregation in steel ingots, *Steel Res. Int.*, 81(2010), No.11, p.994.